

Article

Covalent Modification of Iron Phthalocyanine into Skeleton of Graphitic Carbon Nitride and Its Visible-Light-Driven Photocatalytic Reduction of Nitroaromatic Compounds

Jiajia Qian^{1,2,†}, Ying Liu^{3,†}, Weiran Zheng^{1,*}, Baocheng Zhou³ and Xiaoping Dong^{3,*}

¹ Institute of Agro-Product Safety and Nutrition, Zhejiang Academy of Agricultural Sciences, Hangzhou 310021, China; 13067886408@163.com

² Jiaxing Eco-Environmental Monitoring Center of Zhejiang Province, Jiaxing, 314000, China; liuyingzstu@126.com (Y.L.); zhoubc1982@zstu.edu.cn (B.Z.)

³ Department of Chemistry, Zhejiang Sci-Tech University, Hangzhou 310018, China

* Correspondence: rancki@163.com (W.Z.); xpdong@zstu.edu.cn (X.D.)

† These authors contributed equally to this work.

Abstract: It is of great urgency to eliminate nitroaromatic compounds (NACs) in wastewater due to their high residue and toxicity. Photocatalysis reduction is considered to be an efficient technology for converting NACs to their corresponding aromatic amines. In this work, a visible-light-driven hybrid photocatalyst was synthesized by covalently doping Fe phthalocyanine (FePc) into graphitic carbon nitride skeleton. Compared to the pristine gCN, the optimized gCN-FePc-1 photocatalyst showed enhanced absorption in visible light region, which promoted photogenerated charge transfer and separation. Using *p*-nitrophenol (*p*-NP) as the model pollutant, the CN-FePc-1 effectively reduced it to *p*-aminophenol (*p*-AP), with the photocatalytic reaction rate being 18 and 3 times higher, respectively, than those of the pristine gCN and the mechanically mixed photocatalyst of gCN/FePc. Moreover, excellent photocatalytic universality for other NACs, high stability, and good reusability also were confirmed. Based on the band structure of the gCN-FePc-1 photocatalyst, a plausible mechanism was proposed to illustrate the photocatalytic reduction process of *p*-NP to *p*-AP. This study demonstrates that the covalent modification of FePc into gCN skeleton is an effective strategy to modulate the electronic structure, and the hybrid gCN-FePc is a potential visible-light-driven photocatalyst that potentially can be used for eliminating NAC contamination in wastewater.

Keywords: iron phthalocyanine; graphitic carbon nitride; covalent modification; photocatalytic reduction; nitroaromatic compounds



Citation: Qian, J.; Liu, Y.; Zheng, W.; Zhou, B.; Dong, X. Covalent Modification of Iron Phthalocyanine into Skeleton of Graphitic Carbon Nitride and Its Visible-Light-Driven Photocatalytic Reduction of Nitroaromatic Compounds. *Catalysts* **2022**, *12*, 752. <https://doi.org/10.3390/catal12070752>

Academic Editor: Andres R. Alcantara

Received: 18 June 2022

Accepted: 5 July 2022

Published: 7 July 2022

Publisher's Note: MDPI stays neutral with regard to jurisdictional claims in published maps and institutional affiliations.



Copyright: © 2022 by the authors. Licensee MDPI, Basel, Switzerland. This article is an open access article distributed under the terms and conditions of the Creative Commons Attribution (CC BY) license (<https://creativecommons.org/licenses/by/4.0/>).

1. Introduction

Nitroaromatic compounds (NACs) are one of the most used industrial chemicals. They are classified as one of 129 priority pollutants by the US Environmental Protection Agency due to their extensive application and high toxicity [1,2]. Consequently, effective elimination of NAC residuals in effluent has become an urgent issue in wastewater treatment. However, nitro group has strong electron affinity, and aromatic structure has high stability, making NACs difficult to oxidize [3]. Reduction strategies naturally are considered as potential methods for treating NAC residuals in wastewater, because their reduced products, aromatic amines, are easily degraded and less toxic than NACs [4,5]. Furthermore, aromatic amines are important intermediates in the production of organic chemicals such as dyes, medicaments, rubber, and insecticides [6].

Several approaches have been developed to convert NACs to aromatic amines. Catalytic hydrogenation over noble metals, such as Pt, Pd, Rh, and Au, undoubtedly is the most widely used route in current aromatic amine production [7–9]. However, this approach is drastically limited by the exorbitant cost and poor selectivity of noble metals

despite their superior activity. Zero-valent iron (ZVI) is an environmentally friendly and a low-cost reductant that has been extensively employed to eliminate environmental pollutants, including NACs [4,10]. By receiving electron from ZVI, the nitro group of NACs is directly reduced to amino unit, which, results in the formation of a large amount of iron hydroxide sediments. Photocatalytic reduction technique displays the advantages of economic benefits, green process, and energy-saving property, becoming a potential strategy to remove NAC contaminants from wastewater [11,12].

Recently, environmentally friendly carbon-based photocatalysts, including grapheme quantum dots [13] and covalent organic frameworks [14], have received numerous attention. Compared to other carbon-based photocatalysts, the visible-light-driven (VLD) graphitic carbon nitride (gCN) can be facily prepared from low-cost precursors and thus has become one of the most extensively investigated photocatalytic materials for fuel production and environmental pollution management [15–17]. Unfortunately, its photocatalytic activity is severely suppressed by their limited absorption of sunlight, rapid recombination of photogenerated electron-hole pairs, and poor specific surface area [18–20]. In order to overcome the inherent limitations of gCN, research on bandgap engineering, copolymerization, elemental doping, morphology modulation, and heterojunction construction has been conducted [21–23]. Recently, Fe-doped gCN-based photocatalysts attracted numerous attention due to the high abundance of Fe element in earth's crust and the excellent catalytic activity in both energy and environmental catalysis [24,25]. For example, Tonda et al. reported that Fe atom doping had a significant influence on the electronic structure and catalytic property of gCN [26]. G. Wang et al. synthesized Fe-doped gCN nanosheets using NH_4Cl and FeCl_3 as the raw materials, whose activity was 2.5 times higher than that of the pristine gCN [27]. Due to the poor chelating ability of heptazine unit, C. Yao et al. covalently modified EDTA motif on gCN framework and obtained much higher Fe content [28]. The photocatalytic activity of Fe-EDTA-gCN for nitrogen fixation is twice that of Fe-gCN as photocatalyst.

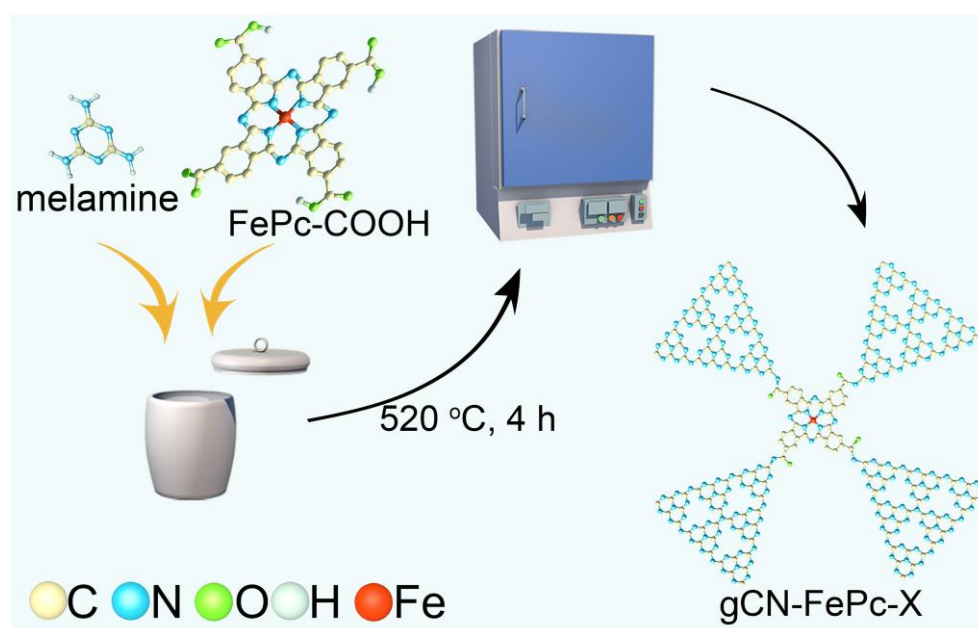
Metal phthalocyanines (MPcs) have become potential photocatalysts because of their controllable compositions, intensive absorption from visible light to near-infrared light, and high charge transfer capability because of aromatic heterocyclic structure [29,30]. However, the π - π effect between molecules leads to the intense agglomeration of MPcs and thus reduce their photocatalytic activity [31,32]. Such aggregation can be effectively avoided by decorating MPcs on other photocatalysts. Various MPcs, including CoPc, ZnPc, FePc, and CuPc, were loaded on gCN, and the obtained MPc/gCN composites displayed enhanced photocatalytic performance [25,33–35]. However, MPcs generally serve as photosensitizer to enlarge the absorption range of photocatalysts in the composite system. Herein, we successfully doped FePc into gCN skeleton through a facile copolymerization route with the precursor melamine. The skeletal modification of gCN with FePc significantly changed the electronic structure of photocatalyst, improved visible light absorption and photogenerated electron reducibility, and promoted charge transfer and separation. By using *p*-nitrophenol (*p*-NP) as the model pollutant of NACs, we evaluated the VLD photocatalytic reduction performance for converting NACs to the corresponding aromatic amines. We also studied the effects of FePc doping content, hydrazine concentration and experimental condition on the activity, photocatalytic universality for other NACs, comparison with the mechanically mixed CN/Pc, and the photocatalytic durability. Finally, we proposed a possible mechanism to explain the strengthened photocatalytic activity.

2. Experimental Section

2.1. Synthesis of Photocatalysts

The pristine gCN was obtained by thermal polymerization with melamine as raw material, which was reported in our previous literature [36,37]. The carboxyl functionalized FePc (FePc-COOH) was obtained using low toxic *o*-phthalic anhydride as precursor, according to the literature [38] (the detailed procedure is given in the Supplementary Material). Additionally, the gCN-FePc-X was synthesized by copolymerization. Typically, 2.0 g of

melamine and 0.01 g of FePc-COOH were mixed and poured into a crucible with a cover and then heated in a muffle furnace at 520 °C for 4 h. After cooling to room temperature, the resultant mixture was ground to powder and denoted as gCN-FePc-1, where “1” represents the FePc-COOH/gCN mass ratio in percentage (the yield of gCN using melamine as precursor was about 50%). To determine the optimum loading content of FePc-COOH, other contents (0.5 wt%, 2 wt%, 4 wt%, 8 wt%, and 16 wt%) were controlled by adding FePc-COOH at different masses, respectively, called gCN-FePc-0.5, gCN-FePc-2, gCN-FePc-4, gCN-FePc-8, and gCN-FePc-16. For comparison, 1.0 g of gCN and 0.01 g of FePc-COOH were mixed and marked as “gCN+FePc-1”. The synthesis diagram of photocatalysts is shown in Scheme 1.



Scheme 1. Schematic diagram of the synthesis of gCN-FePc-X.

2.2. Characterizations

The morphology and element distribution of the samples were obtained on a SU-8100 field emission scanning electron microscope (SEM, Hitachi, Naka, Japan) equipped with an energy dispersive X-ray spectrometer (EDS, iXRF, Austin, TX, USA). The transmission electron microscopy (TEM) observation was performed on a JEM-2100 electron microscope (JEOL, Tokyo, Japan) operating at an accelerating voltage of 200 kV. The lattice structures of the materials were characterized by powder X-ray diffraction (XRD, DX-2700, Dadong, China). Fourier transform infrared spectra (FTIR) were recorded on an Avatar 370 spectrophotometer (Thermo Nicolet, Madison, Wisconsin, WI, USA). UV-vis diffuse reflectance spectra (DRS) and absorption spectra were measured on a UV-vis spectrometer (Shimadzu UV-2450, Suzhou, China). Steady-state photoluminescence (PL) spectra, where the excitation wavelength was 340 nm, and time-resolved transient PL decay of the solid photocatalysts, where the emission wavelength was 460 nm, were measured on a FluoroMax-4 fluorescence spectrometer (Horiba, Piscataway, New Jersey, NJ, USA).

2.3. Photocatalytic Tests

Firstly, the VLD photocatalytic reduction activity of photocatalysts was evaluated using *p*-nitrophenol (*p*-NP) as a model pollutant of NACs. A 300 W Xe lamp equipped with a 420 nm cutoff filter was employed as light resource. In a detailed reaction procedure, 100 mg of photocatalyst was dispersed into 100 mL *p*-NP solution (5 mg L⁻¹) containing 0.04 M N₂H₄ and magnetic stirring was performed. After 30 min of dark adsorption, the adsorption–desorption equilibrium was established, and xenon lamp was turned on to start the photocatalytic reaction. A total of 2 mL suspension was sampled every 20 min,

followed by centrifugation at 12,000 rpm for 5 min and filtration using a 0.22 μm membrane to remove photocatalyst. Then, the resultant clean solution was analyzed by a UV-vis spectrometer (Shimadzu UV-2450). All the experimental data is the average values of three repeated experiments. In addition, *p*-NP and its reduced product *p*-aminophenol (*p*-AP) were further analyzed by a high-performance liquid chromatography (HPLC, Shimadzu LC-20A, Suzhou, China) system equipped with a WondaSil C18 (4.6–200 mm, 5 μm). The buffer solution was 10 mM KH_2PO_4 , the pH of which was adjusted to 2.5 with H_3PO_4 , the volumetric ratio of CH_3OH and KH_2PO_4 was 11:9, and the flow rate was 1.0 mL min^{-1} . Other NACs, such as *o*-nitrophenol (*o*-NP), *m*-nitrophenol (*m*-NP), nitrobenzene (NB), *p*-chloronitrobenzene (*p*-Cl-NB), *p*-bromonitrobenzene (*p*-Br-NB), and *p*-nitrobenzoic acid (*p*-COOH-NB), also were used to evaluate the photocatalytic reduction performance of the obtained catalysts. The reaction procedures were similar to that of *p*-NP.

2.4. Electrochemical Measurements

Electrochemical tests were performed on an electrochemical workstation (CHI660E, Chenhua, Shanghai, China) using 0.5 M Na_2SO_4 solution as the electrolyte solution, Pt foil as the counter electrode, and Ag/AgCl as the reference electrode. The working electrode was prepared following the below procedure: A total of 25 mg of photocatalyst was dispersed in 1 mL of 5 wt% polyvinylidene fluoride (PVDF) solution and then coated on a 3 cm \times 1 cm ITO conductive glass by spin-coating technology. Electrochemical impedance spectra (EIS) were recorded in the frequency range from 0.1 Hz to 100,000 Hz with a 10 mV AC voltage. Mott-Schottky plots in the frequencies of 500 Hz, 1,000 Hz, and 1,500 Hz were obtained.

3. Results and Discussion

3.1. Morphology and Structure

The surface morphologies and microstructures of gCN and gCN-FePc-1 were characterized by SEM and TEM (Figure 1a–d). The SEM images show that there was no obvious difference in the morphology between gCN and gCN-FePc-1; both have an irregular granular shape. Additionally, a typically layered structure was observed in their TEM images. The gCN-FePc-1 is much thinner than the gCN. The curl of thin layer is shaded in a wire-like dark zone in Figure 1d, which indicates that the Van der Waals force between gCN sheets could be reduced by introducing FePc into the gCN skeleton, thus leading to the formation of thin flakes. Additionally, no particles were seen on the sample surface, suggesting FePc had been successfully doped into skeleton in molecule level. The EDS elemental mapping of gCN-FePc-1 in Figure S1 shows that the distribution of Fe element was in accordance with those of C, N, and O elements, which demonstrates that the phthalocyanine chelated Fe (III) complex was evenly distributed in the gCN framework.

Figure 2a displays XRD patterns of samples. The pattern of the prepared gCN implies that it demonstrated a good purity without any secondary or impurity phase, and the two respective peaks centered at 13.3° (100) and 27.6° (002) are attributed to the in-plane structural packing of tri-s-triazine motifs and repeated inter-planar stacking of conjugated aromatic systems, respectively [39–41]. After FePc was introduced into the gCN skeleton, these two diffractions remained in the gCN-FePc-X samples, but the crystallinity gradually decreased with the increase in the FePc content due to the gradual increase in full width at half maximum (FWHM). That should be ascribed to the partial destruction of periodic arrangement of tri-s-triazine units. The pure FePc-COOH exhibited an obvious diffraction at $\sim 27.4^\circ$ [32,42]. We can find from the enlarged XRD patterns within the range of 26–29° (Figure 2b) that the (002) peak of graphite-like structure in gCN-FePc-X samples gradually shifts to low 2θ value with the increase in the FePc content, which potentially originated from the disturbance of the graphitic structure caused by modifying FePc into the CN framework, thus enlarging the interlayer distance.

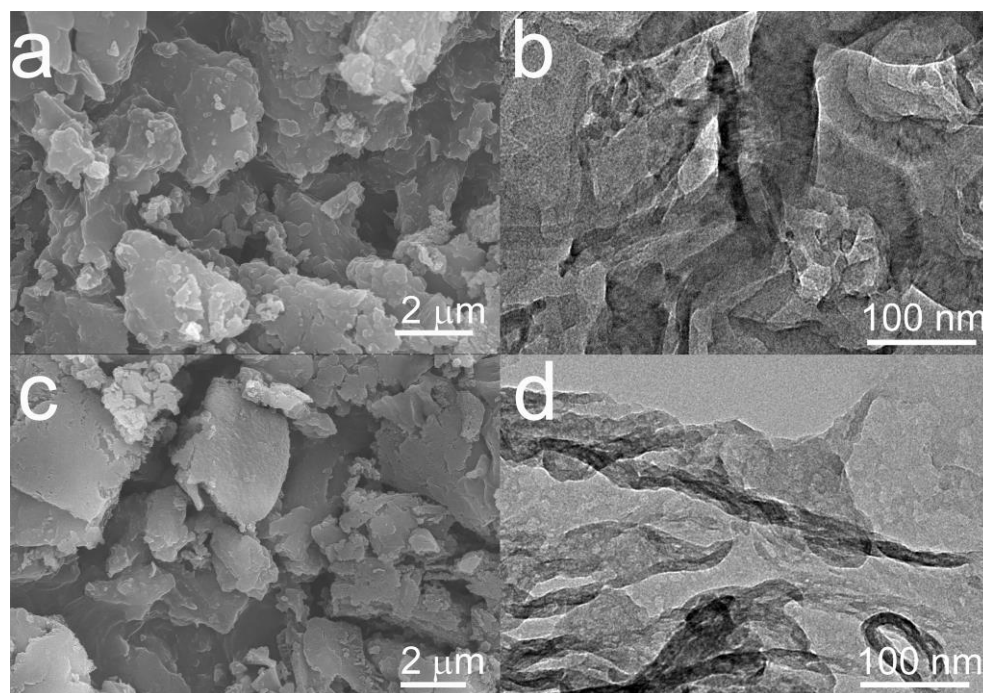


Figure 1. SEM and TEM images of gCN (a,b) and gCN-FePc-1 (c,d).

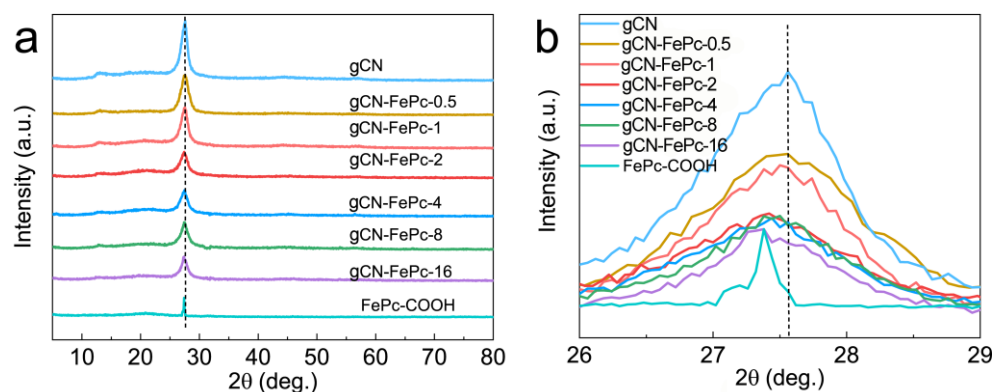


Figure 2. XRD patterns of different samples (a) and the enlarged region of 26–29° (b).

Functional groups on photocatalysts were characterized through FTIR technology, and the results are illustrated in Figure 3. Broad absorption band at $\sim 3450\text{ cm}^{-1}$ was related to the stretching vibration of O–H from adsorption water and that at $\sim 3200\text{ cm}^{-1}$ was contributed to the N–H vibration of the terminal amino group on gCN. Compared to the gCN and FePc-COOH, the change in the relative intensity of such absorption in the gCN-FePc-1 suggests the well hybridization of gCN and FePc. A series of characteristic absorption at $1800\text{--}1200\text{ cm}^{-1}$ was assigned to the typical stretching vibrations of C–N heterocycles and at 810 cm^{-1} to the breathing mode of s-triazine ring [43–45]. The spectrum of FePc-COOH showed that the strong absorption band at 1604 cm^{-1} corresponded to the stretching vibration of –COOH group and the C–N heterocyclic ring; the absorption at 1362 cm^{-1} and 1249 cm^{-1} to the C=C vibrations of aromatic ring and the peaks at 808 cm^{-1} and 773 cm^{-1} originated from the skeleton vibration of phthalocyanine, respectively [31,42]. These characteristic absorption of FePc were observed in the gCN-FePc-1 sample, implying the successful formation of hybrid photocatalyst.

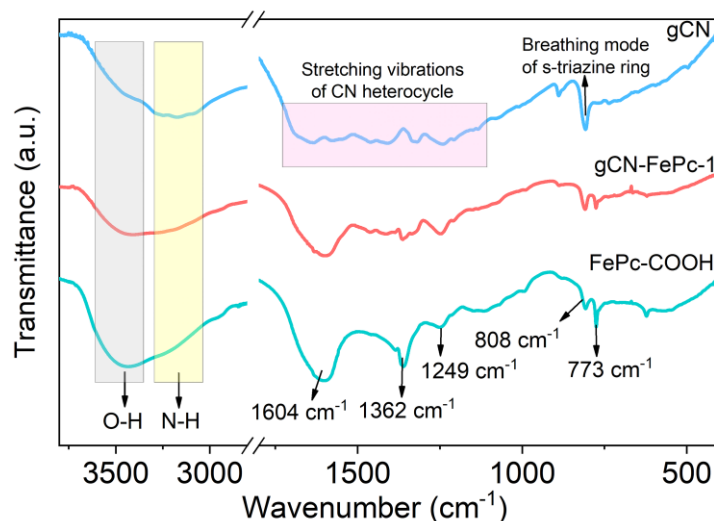


Figure 3. FTIR spectra of different samples.

3.2. Optical Properties

Optical properties of the as-prepared gCN and gCN-FePc-1 samples were examined using UV-vis DRS technology. As shown in Figure 4a, the strong absorption in the UV region of gCN-FePc-1 was attributed to band-to-band transition. The gCN demonstrated an absorption edge of ~ 460 nm, but with incorporation of FePc, a significant broad absorption band in visible light region was clearly observed in the spectrum of gCN-FePc-1 sample, which could be induced by the absorptions of B-band and Q-band of FePc, as well as the ligand-to-metal charge transfer (LMCT) transition [22]. The existence of LMCT indicates that the FePc had an electron-withdrawing effect, which effectively prevented the recombination of photogenerated carriers and improved the photocatalytic performance.

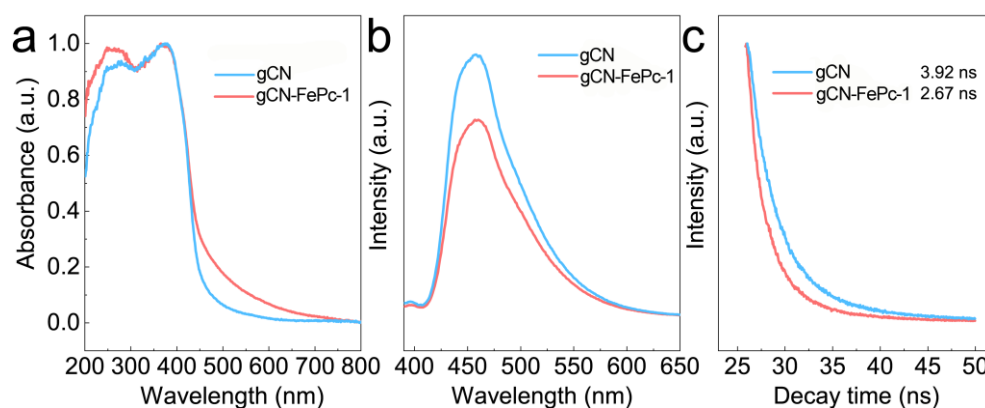


Figure 4. UV-vis DRS (a), steady-state PL spectra (b), and time-resolved PL spectra (c) of gCN and gCN-FePc-1.

The photocatalytic activity of gCN was suppressed due to the high recombination ratio of photogenerated electron-hole pairs, leading to the generation of strong PL emission (as seen in Figure 4b). The PL intensity decreased evidently after coupling FePc on gCN, demonstrating the electron-hole recombination was suppressed in gCN-FePc-1 [46]. The time-resolved PL spectra of gCN and gCN-FePc-1 also were examined (Figure 4c), and the fluorescence lifetimes were calculated to be 3.92 ns for gCN and 2.67 ns for gCN-FePc-1. The decrease in time-resolved PL lifetime indicated a more effective conversion of singlet exciton in the photocatalyst and charge transfer kinetics [47,48].

3.3. XPS Analysis

The XPS survey spectrum of gCN-FePc-1 (Figure S2) suggests that the hybrid photocatalyst contains C, N, O, and Fe elements. The C 1s spectra (Figure 5a) depict two main peaks located at the binding energies of 287.5 eV and 284.6 eV, respectively, attributed to the existence of C element in the aromatic skeleton rings of $\text{N}=\text{C}-(\text{N})_2$ and sp^2 $\text{C}-\text{C}=\text{C}$ bonds [46,49]. The enhanced relative intensity of the $\text{C}-\text{C}=\text{C}$ motif was ascribed to the doping of FePc in the hybrid. In addition to these two peaks, an additional peak at 287.2 eV was observed in the spectrum of gCN-FePc-1 sample and contributed to the $-\text{NH}-\text{CO}-$ group that was formed by reacting amino group on melamine with carboxyl group of FePc-COOH [50]. Figure 5b compares the N 1s spectra of gCN and gCN-FePc-1. The gCN spectrum was fitted into three signals at 401.2, 399.4 and 398.0 eV, respectively, representing the N elements in $\text{N}-\text{H}$, $\text{N}-(\text{C})_3$ and the conjugated $\text{C}=\text{N}-\text{C}$ unit [51,52]. Similarly, the additional peak at 400.4 eV in the gCN-FePc-1 sample was ascribed to the N atom of amide group [53,54]. The O 1s spectrum of gCN-FePc-1 (Figure 5c) contained two peaks. The absorption at 532.0 eV was similar to the signal of gCN from adsorbed water on surface and that at 533.1 eV resulted from the O atom of amide group [55]. The Fe 2p spectrum of gCN-FePc-1 (see Figure 5d) presents two characteristic peaks, where the signal at 725.8 eV originated from $\text{Fe } 2\text{p}_{1/2}$, and the absorption at 711.6 eV was related to $\text{Fe } 2\text{p}_{3/2}$ of trivalent iron ion [56,57].

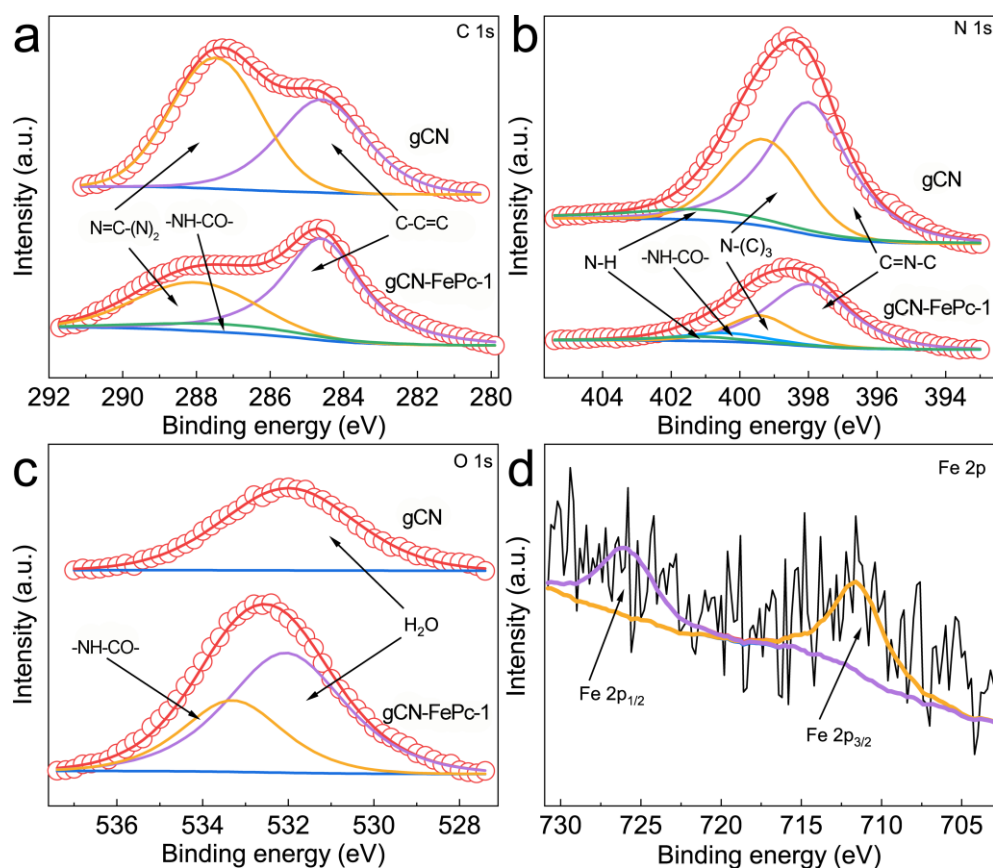


Figure 5. XPS spectra of gCN and gCN-FePc-1: C 1s (a), N 1s (b), O 1s (c), and Fe 2p (d).

3.4. VLD Photocatalytic Performance for Reduction in NACs

We firstly investigated the photocatalytic activity of photocatalysts for the reduction in NACs through using *p*-NP as the model pollutant. As described in Figure S3, aqueous solution of *p*-NP showed an absorption peak centered at 316 nm, and the peak shifted to 400 nm in the presence of N_2H_4 due to the transformation of *p*-NP to *p*-nitrophenolate ion under the acid-base reaction of acidic phenol hydroxyl group and alkaline hydrazine [58].

With the VLD photocatalysis by gCN-FePc-1, the intensity of absorption at 400 nm decreased gradually, while a new absorption at 297 nm indexed to *p*-AP gradually increased (see Figure 6a). To further ensure the formation of *p*-AP as a product of *p*-NP reduction, the reaction solution was detected with HPLC (Figure S4). The two peaks were assigned to *p*-NP (retention time of 4.46 min) and *p*-AP (retention time of 2.46 min) in these HPLC spectra, respectively, which demonstrate that no by-products were produced. In the HPLC spectrum of reaction solution irradiated for 140 min, the signal disappeared at 4.46 min, indicating all *p*-NP had been converted to *p*-AP. Figure 6b compares the photocatalytic conversion of *p*-NP under different photocatalysts. Compared to the gCN, all gCN-FePc-X catalysts displayed enhanced photocatalytic behavior, among which the gCN-FePc-1 possessed the best photocatalytic activity.

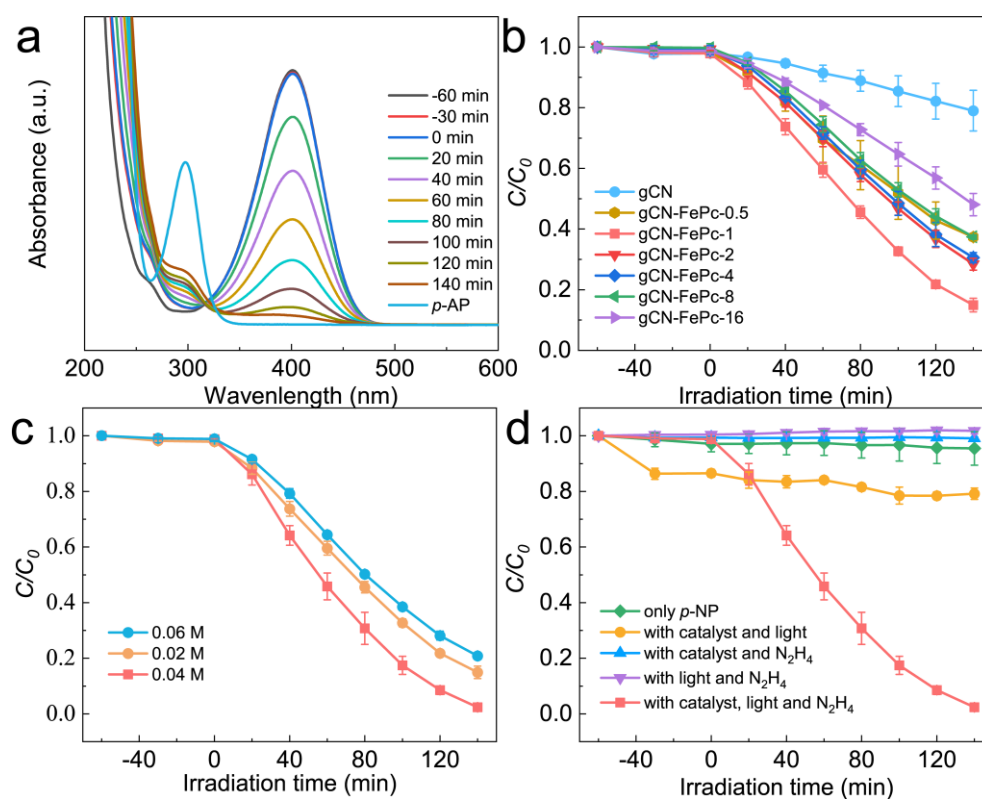


Figure 6. UV-vis absorption spectra of *p*-NP solution after photocatalytic reaction by the gCN-FePc-1 from 0–140 min (a); comparison of photocatalytic performance for *p*-NP reduction by various photocatalysts (b); effect of N_2H_4 dosage on photocatalytic reduction activity of *p*-NP by gCN-FePc-1 (c); photocatalytic reduction performance of *p*-NP under various experimental conditions (d). The experimental data in Figure 6 (b–d) are based on three repeated experiments.

Hydrazine acted as an electron and proton donor in this photocatalytic process; therefore, its concentration plays an important role. We studied the photocatalytic activity of gCN-FePc-1 photocatalyst using three N_2H_4 concentrations (0.02 M, 0.04 M, and 0.06 M, see Figure 6c). When the concentration increased from 0.02 M to 0.04 M, the *p*-NP reduction reaction was accelerated. However, as N_2H_4 concentration further increased to 0.06 M, the *p*-NP conversion was drastically suppressed. The reason may be that a low N_2H_4 concentration is insufficient to quench the photoexcited hole on the valance band (VB) of photocatalyst, while excessive N_2H_4 molecules will occupy the photocatalyst surface to limit the electron transfer from the conduction band (CB) of photocatalyst to the *p*-NP. Figure 6d shows the photocatalytic behavior of *p*-NP reduction under different reaction conditions. In the absence of one factor among visible light irradiation, photocatalyst and hydrazine could not drive the reduction in *p*-NP, demonstrating that these three factors were vital for such reaction. Meanwhile, no reduced product *p*-AP signal could be found in

the HPLC spectra (Figure S5 and Table S1) under the above reaction conditions, further confirming the above results.

The activity of gCN-FePc-1 for photocatalytic reduction in other NACs to their corresponding amino-aromatic compounds also was investigated, and the conversion is listed in Table 1. Table 1 shows that NACs substituted by different groups, including *o*-NP, *m*-NP, NB, *p*-Cl-NB, *p*-Br-NB, and *p*-COOH-NB, could be converted into their corresponding aromatic amines with a high conversion (>95%) by the photocatalytic reaction of gCN-FePc-1 under visible light irradiation.

Table 1. HPLC determined composition of the reaction solutions before and after the gCN-FePc-1 photocatalysis.

Entry	Substrate	Reduced Product	Conversion (%)
1			97
2			98
3			98
4			98
5			99
6			99
7			99

The experimental data in Table 1 are based on three repeated experiments.

Photocatalytic activity of the optimal FePc covalently modified gCN photocatalyst, gCN-FePc-1, was compared with that of the gCN+PcFe-1 sample prepared by mechanically mixing gCN and FePc with the same FePc concentration to the gCN-FePc-1 (Figure 7a). The results showed that the *p*-NP conversion rate of gCN+FePc-1 was 66% under 140 min VLD photocatalytic condition, which was much higher than that of the pristine gCN; the *p*-NP conversion rate was 17% under the same irradiation time. The *p*-NP conversion of the gCN-FePc-1 photocatalyst was up to 98%, further improving the performance. Figure 7b shows the fitted curves of photocatalytic data using the first-order kinetic equation. The figure shows the apparent rate constant (k) of gCN-FePc-1 was $2.0 \times 10^{-2} \text{ min}^{-1}$, 18 and 3 times higher than those of the gCN and gCN+FePc-1 samples, respectively, which suggests that the light absorption and charge transfer and separation could be more effectively promoted by doping FePc into gCN than by mechanically mixing FePc with gCN. Furthermore, the photocatalytic durability of gCN-FePc-1 was evaluated, as shown in Figure 7c. In the successive five runs, the gCN-FePc-1 demonstrated similar efficiencies (95~98%), illustrating its superior reusability. The used photocatalyst was recycled and measured by XRD technology (Figure 7d). The pattern of the recycled photocatalyst had similar peaks to that of the fresh gCN-FePc-1, demonstrating its high structural stability.

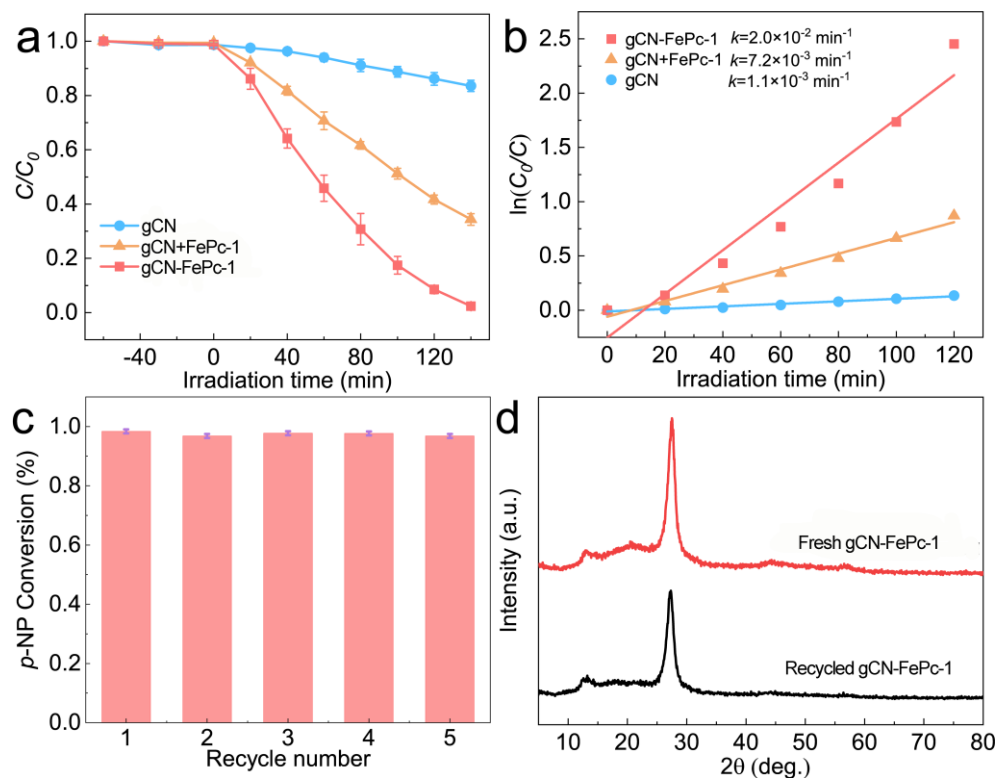


Figure 7. Photocatalytic reduction in *p*-NP over different photocatalysts under visible light irradiation (a); the corresponding pseudo-first-order kinetic curves and the apparent rate constants (b); cycle stability test of gCN-FePc-1 (c); XRD patterns (d) of the fresh gCN-FePc-1 and the recycled gCN-FePc-1. The experimental data in Figure 7 (a–c) are based on three repeated experiments.

3.5. Plausible Photocatalytic Mechanism

Semiconductors with intrinsic bandgap structures are known to possess reliable photoelectric conversion properties. In order to demonstrate the enhanced photoelectric performance after the addition of FePc into CN skeleton, the transient photocurrent response and EIS were measured. As presented in Figure 8a, the gCN-FePc-1 exhibited much higher photocurrent intensity than the gCN, indicating that much more photoexcited electron-hole pairs were generated and separated in the gCN-FePc-1 [24,59]. The EIS spectrum in Figure 8b shows that the gCN-FePc-1 possessed a smaller arc radius than gCN, representing a lower resistance and a higher charge transfer ability in the gCN-FePc-1 than the gCN [19,60].

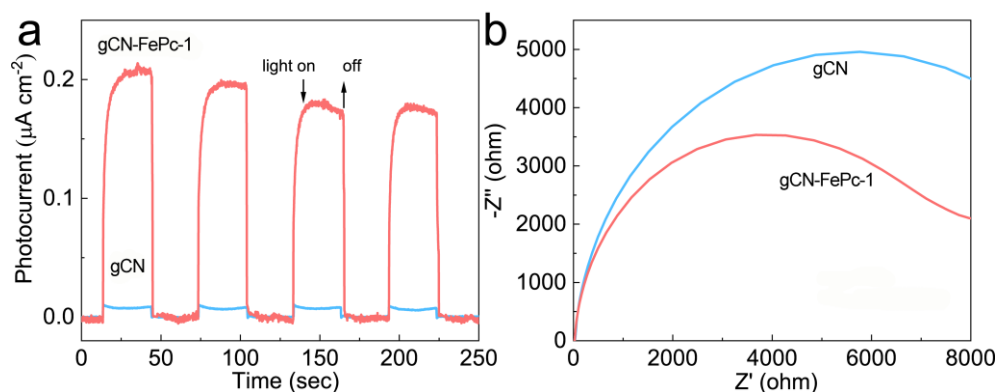


Figure 8. Transient photocurrent responses (a) and EIS plots (b) of samples.

To better understand the enhanced photocatalytic performance of gCN-FePc-1, the band structure was determined (see Figure 9). The flat-band potential (V_{fb} , generally regarded as the Fermi level, E_f) was determined by the Mott–Schottky (MS) equation [61]:

$$\frac{1}{C^2} = \left(\frac{2}{\epsilon_r \epsilon_0 N_d e} \right) \times \left(V - V_{fb} - \frac{k_B T}{e} \right) \quad (1)$$

where C is the depletion layer capacitance, ϵ_r is the dielectric constant of semiconductor, ϵ_0 is the vacuum permittivity, N_d is the carrier donor density, V is the applied potential, and $k_B T/e$ is the temperature-dependent correction term. Both gCN and gCN-FePc-1 are n-type semiconductors due to their positive slopes (Figure 9a), whose E_f values relative to Ag/AgCl are -1.20 V and -1.25 V, converted into reversible hydrogen electrode (RHE) potential by the following the formula [36,62]:

$$E_{RHE} = E_{Ag/AgCl} + 0.198 \text{ eV} + 0.0592 \text{ pH} \quad (2)$$

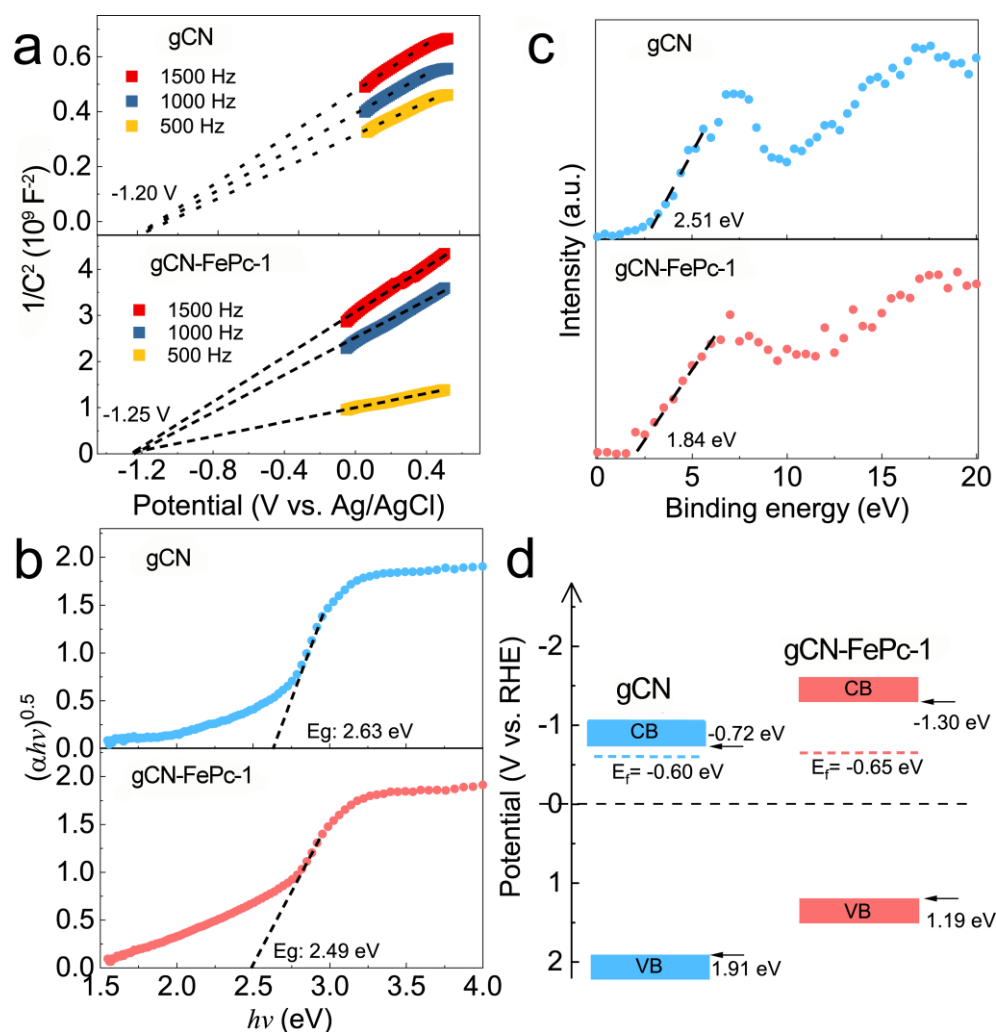


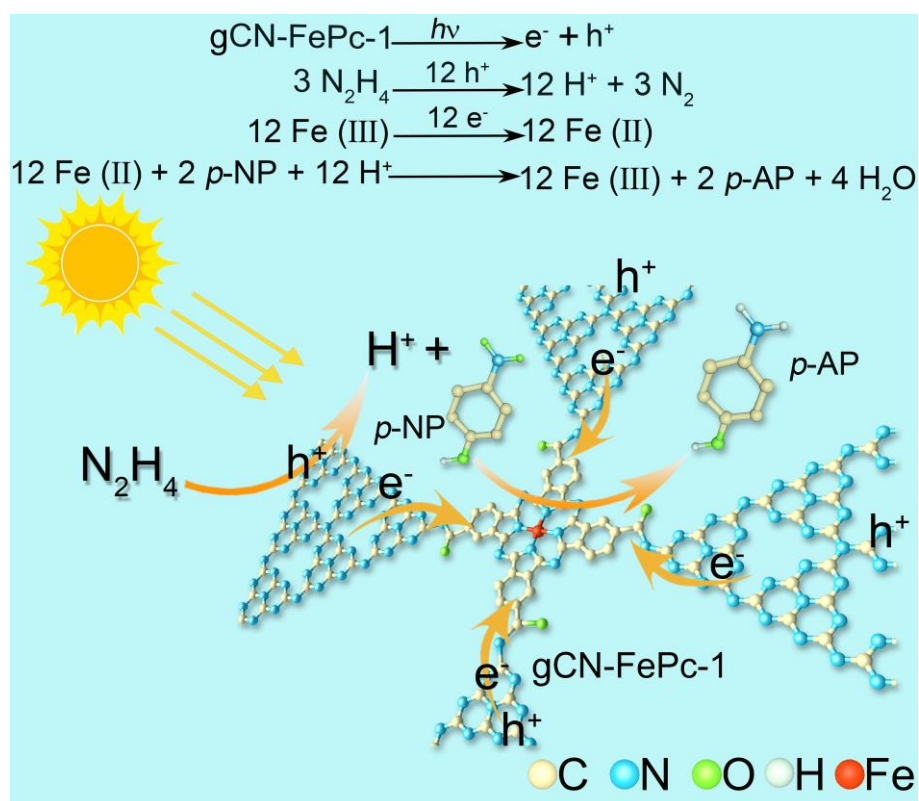
Figure 9. Mott–Schottky curves (a), Tauc plots (b), XPS VB spectra (c), and band structure (d) of gCN and gCN-FePc-1.

Among them, the pH of the $0.5 \text{ M Na}_2\text{SO}_4$ electrolyte solution is 6.8; therefore, we calculated the E_f of gCN and gCN-FePc-1 to be -0.60 eV and -0.65 eV vs. RHE, respectively. The bandgap was measured via the Tauc plot (Figure 9b) by converting the DRS data using the Kubelka–Munk equation:

$$\alpha h\nu = k(E_g - h\nu)^{n/2} \quad (3)$$

where α is absorption coefficient, k is a constant, h is Planck constant, ν is frequency of the incident light, E_g is bandgap, and n is equal to 1 for direct bandgap semiconductor or 4 indirect bandgap semiconductor. Since graphitic carbon nitride is an indirect bandgap semiconductor, the bandgap values of gCN and gCN-FePc-1 were calculated to be 2.63 eV and 2.49 eV. The relative potentials between the VB and the E_f obtained by XPS VB spectra (Figure 9c) were 2.51 eV for gCN and 1.84 eV for gCN-FePc-1. Based on the above results, the CB/VB values of both gCN and gCN-FePc-1 were calculated to -0.72 eV/ 1.91 eV and -1.30 eV/ 1.19 eV, respectively, and the band structure diagram of the materials is shown in Figure 9d. By comparison, it is found that the gCN-FePc-1 had a much higher CB edge potential than the pristine gCN, which means the photogenerated electrons on the CB of gCN-FePc-1 had much stronger reducibility. In addition, the gap between the E_f and the CB on the gCN-FePc-1 was larger than that on the gCN, suggesting that the density of electron cloud on the CN framework could be reduced by modifying FePc with electron-withdrawing ability.

Based on the above results, we proposed a possible mechanism of gCN-FePc-1 for photocatalytic reduction in *p*-NP with hydrazine (Scheme 2). Under visible light illumination by xenon lamp, electrons on the VB of gCN-FePc-1 were excited and transmitted to its CB, leaving holes on the VB. The photogenerated electrons were transferred to the FePc unit due to its electron-withdrawing property. These surface holes with strong oxidative ability were captured by hydrazine to produce N_2 and H^+ [1]. However, the Fe (III) was reduced to Fe (II) by the photoexcited electron. Subsequently, Fe (II) was oxidized to Fe (III) by amination of protons produced by hydrazine at the active site of Fe.



Scheme 2. Possible photocatalytic mechanism for *p*-NP reduction by the gCN-FePc-1 under visible light irradiation.

4. Conclusions

In summary, a highly efficient VLD photocatalytic route was developed to reduce and eliminate NACs using the gCN photocatalyst covalently modified by FePc. Through various characterization technologies, the improved visible light absorption and the promoted

charge transfer and separation ability were confirmed. The content of FePc in the hybrid was optimized. The results indicate that the gCN-FePc-1 demonstrates the best activity. The photocatalytic reduction rate of *p*-NP is 18 and 3 times higher than those of the pristine gCN and the mechanically mixed gCN+FePc-1, respectively. Moreover, the gCN-FePc-1 has good photocatalytic reusability and superb reducing activity to other NACs. In addition, such efficient separation and strong redox property of the photogenerated charge carriers imply that gCN-FePc-1 is potentially applicable to other organic synthesis and pollution control.

Supplementary Materials: The following supporting information can be downloaded at <https://www.mdpi.com/article/10.3390/catal12070752/s1>. Synthesis of carboxyl functionalized FePc; Figure S1: EDS element mapping of gCN-FePc-1; Figure S2: The XPS survey spectrum of gCN-FePc-1; Figure S3: UV-vis absorption spectra of *p*-NP solution before and after adding N₂H₄; Figure S4: The liquid chromatograms of *p*-NP solution after photocatalytic reaction, the initial *p*-NP solution and the *p*-AP standard solution; Figure S5: The liquid chromatograms of *p*-NP solutions before and after different treatments; Table S1: The composition of *p*-NP solutions before and after different conditions analyzed by HPLC.

Author Contributions: Conceptualization, W.Z. and X.D.; methodology, J.Q. and Y.L.; validation, J.Q., Y.L. and B.Z.; formal analysis, J.Q. and Y.L.; investigation, J.Q. and Y.L.; writing—original draft preparation, J.Q.; writing—review and editing, W.Z. and X.D.; visualization, B.Z. and W.Z.; supervision, W.Z. and X.D.; project administration, X.D.; funding acquisition, X.D. All authors have read and agreed to the published version of the manuscript.

Funding: This research was funded by the Zhejiang Provincial Natural Science Foundation of China, grant number LY20B070001.

Conflicts of Interest: The authors declare no conflict of interest.

References

1. Liu, J.; Li, J.; Meng, R.; Jian, P.; Wang, L. Silver nanoparticles-decorated-Co₃O₄ porous sheets as efficient catalysts for the liquid-phase hydrogenation reduction of *p*-nitrophenol. *J. Colloid Interf. Sci.* **2019**, *551*, 261–269. [CrossRef] [PubMed]
2. Mei, X.; Liu, J.; Guo, Z.; Li, P.; Bi, S.; Wang, Y.; Yang, Y.; Shen, W.; Wang, Y.; Xiao, Y.; et al. Simultaneous *p*-nitrophenol and nitrogen removal in PNP wastewater treatment: Comparison of two integrated membrane-aerated bioreactor systems. *J. Hazard. Mater.* **2019**, *363*, 99–108. [CrossRef] [PubMed]
3. Wang, C.; Shen, J.; Chen, R.; Cao, F.; Jin, B. Self-assembled BiOCl/Ti₃C₂T composites with efficient photo-induced charge separation activity for photocatalytic degradation of *p*-nitrophenol. *Appl. Surf. Sci.* **2020**, *519*, 146175. [CrossRef]
4. Shi, D.; Zhu, G.; Zhang, X.; Zhang, X.; Li, X.; Fan, J. Ultra-small and recyclable zero-valent iron nanoclusters for rapid and highly efficient catalytic reduction of *p*-nitrophenol in water. *Nanoscale* **2019**, *11*, 1000–1010. [CrossRef]
5. Bai, X.; Chen, D.; Li, Y.; Yang, X.; Zhang, M.; Wang, T.; Zhang, X.; Zhang, L.; Fu, Y.; Qi, X.; et al. Two-dimensional MOF-derived nanoporous Cu/Cu₂O networks as catalytic membrane reactor for the continuous reduction of *p*-nitrophenol. *J. Membr. Sci.* **2019**, *582*, 30–36. [CrossRef]
6. Huang, T.; Fu, Y.; Peng, Q.; Yu, C.; Zhu, J.; Yu, A.; Wang, X. Catalytic hydrogenation of *p*-nitrophenol using a metal-free catalyst of porous crimped graphitic carbon nitride. *Appl. Surf. Sci.* **2019**, *480*, 888–895. [CrossRef]
7. Cui, Y.; Ma, K.; Chen, Z.; Yang, J.; Geng, Z.; Zeng, J. Atomic-level insights into strain effect on *p*-nitrophenol reduction via Au@Pd core-shell nanocubes as an ideal platform. *J. Catal.* **2020**, *381*, 427–433. [CrossRef]
8. Ye, W.; Yu, J.; Zhou, Y.; Gao, D.; Wang, D.; Wang, C.; Xue, D. Green synthesis of Pt-Au dendrimer-like nanoparticles supported on polydopamine-functionalized graphene and their high performance toward 4-nitrophenol reduction. *Appl. Catal. B Environ.* **2016**, *181*, 371–378. [CrossRef]
9. Cho, H.; Kwon, Y.; Lee, Y.; Park, Y.; Ji, H.; Lee, J. Morphological control of gold nanoparticles on exfoliated layers of layered double hydroxide: A reusable hybrid catalyst for the reduction of *p*-nitrophenol. *Appl. Clay Sci.* **2018**, *156*, 187–194. [CrossRef]
10. Bae, S.; Gim, S.; Kim, H.; Hanna, K. Effect of NaBH₄ on properties of nanoscale zero-valent iron and its catalytic activity for reduction of *p*-nitrophenol. *Appl. Catal. B Environ.* **2016**, *182*, 541–549. [CrossRef]
11. Xiao, G.; Li, P.; Zhao, Y.; Xu, S.; Su, H. Visible-light-driven chemoselective hydrogenation of nitroarenes to anilines in water through graphitic carbon nitride metal-free photocatalysis. *Chem. Asian J.* **2018**, *13*, 1950–1955. [CrossRef] [PubMed]
12. Wu, J.; Wang, J.; Wang, T.; Sun, L.; Du, Y.; Li, Y.; Li, H. Photocatalytic reduction of *p*-nitrophenol over plasmonic M (M = Ag, Au)/SnNb₂O₆ nanosheets. *Appl. Surf. Sci.* **2019**, *466*, 342–351. [CrossRef]

13. Jiang, J.; Ye, G.; Wang, Z.; Lu, Y.; Chen, J.; Matyjaszewski, K. Heteroatom-doped carbon dots (CDs) as a new class of metal-free photocatalysts for PET-RAFT polymerization under visible light and sunlight. *Angew. Chem. Int. Ed.* **2018**, *130*, 12213–12218. [[CrossRef](#)]
14. Zhu, Y.; Zhu, D.; Chen, Y.; Yan, Q.; Liu, C.Y.; Ling, K.; Liu, Y.; Lee, D.; Wu, X.; Senftle, T.P.; et al. Porphyrin-based donor-acceptor COFs as efficient and reusable photocatalysts for PET-RAFT polymerization under broad spectrum excitation. *Chem. Sci.* **2021**, *12*, 16092–16099. [[CrossRef](#)]
15. Ismael, M. A review on graphitic carbon nitride (g-C₃N₄) based nanocomposites: Synthesis, categories, and their application in photocatalysis. *J. Alloy Compd.* **2020**, *846*, 156446. [[CrossRef](#)]
16. Raaja Rajeshwari, M.; Kokilavani, S.; Sudheer Khan, S. Recent developments in architecturing the g-C₃N₄ based nanostructured photocatalysts: Synthesis, modifications and applications in water treatment. *Chemosphere* **2022**, *291*, 132735. [[CrossRef](#)]
17. Liu, J.; Fu, W.; Liao, Y.; Fan, J.; Xiang, Q. Recent advances in crystalline carbon nitride for photocatalysis. *J. Mater. Sci. Technol.* **2021**, *91*, 224–240. [[CrossRef](#)]
18. Hu, X.; Li, Y.; Wei, X.; Wang, L.; She, H.; Huang, J.; Wang, Q. Preparation of double-layered Co-Ci/NiFeOOH co-catalyst for highly meliorated PEC performance in water splitting. *Adv. Powder Mater.* **2022**, *1*, 100024. [[CrossRef](#)]
19. Bellamkonda, S.; Shanmugam, R.; Gangavarapu, R. Extending the π -electron conjugation in 2D planar graphitic carbon nitride: Efficient charge separation for overall water splitting. *J. Mater. Chem. A* **2019**, *7*, 3757–3771. [[CrossRef](#)]
20. Sun, P.; Yu, H.; Liu, T.; Li, Y.; Wang, Z.; Xiao, Y.; Dong, X. Efficiently photothermal conversion in a MnOx-based monolithic photothermocatalyst for gaseous formaldehyde elimination. *Chin. Chem. Lett.* **2022**, *33*, 2564–2568. [[CrossRef](#)]
21. Huang, R.; Wu, J.; Zhang, M.; Liu, B.; Zheng, Z.; Luo, D. Strategies to enhance photocatalytic activity of graphite carbon nitride-based photocatalysts. *Mater. Des.* **2021**, *210*, 110040. [[CrossRef](#)]
22. Gao, C.; Wang, J.; Xu, H.; Xiong, Y. Coordination chemistry in the design of heterogeneous photocatalysts. *Chem. Soc. Rev.* **2017**, *46*, 2799–2823. [[CrossRef](#)] [[PubMed](#)]
23. Yi, J.; El-Alami, W.; Song, Y.; Li, H.; Ajayan, P.; Xu, H. Emerging surface strategies on graphitic carbon nitride for solar driven water splitting. *Chem. Eng. J.* **2020**, *382*, 122812. [[CrossRef](#)]
24. Wei, Y.; Chen, L.; Chen, H.; Cai, L.; Tan, G.; Qiu, Y.; Xiang, Q.; Chen, G.; Lau, T.C.; Robert, M. Highly efficient photocatalytic reduction of CO₂ to CO by in situ formation of a hybrid catalytic system based on molecular iron quaterpyridine covalently linked to carbon nitride. *Angew. Chem. Int. Ed. Engl.* **2022**, *61*, e202116832. [[CrossRef](#)] [[PubMed](#)]
25. Chen, X.; Lu, W.; Xu, T.; Li, N.; Zhu, Z.; Wang, G.; Chen, W. Visible-light-assisted generation of high-valent iron-oxo species anchored axially on g-C₃N₄ for efficient degradation of organic pollutants. *Chem. Eng. J.* **2017**, *328*, 853–861. [[CrossRef](#)]
26. Tonda, S.; Kumar, S.; Kandula, S.; Shanker, V. Fe-doped and-mediated graphitic carbon nitride nanosheets for enhanced photocatalytic performance under natural sunlight. *J. Mater. Chem. A* **2014**, *2*, 6772–6780. [[CrossRef](#)]
27. Gao, J.; Wang, Y.; Zhou, S.; Lin, W.; Kong, Y. A facile one-step synthesis of Fe-doped g-C₃N₄ nanosheets and their improved visible-light photocatalytic performance. *Chemcatchem* **2017**, *9*, 1708–1715. [[CrossRef](#)]
28. Yao, C.; Wang, R.; Wang, Z.; Lei, H.; Dong, X.; He, C. Highly dispersive and stable Fe³⁺ active sites on 2D graphitic carbon nitride nanosheets for efficient visible-light photocatalytic nitrogen fixation. *J. Mater. Chem. A* **2019**, *7*, 27547–27559. [[CrossRef](#)]
29. Zheng, J.; Li, X.; Qin, Y.; Zhang, S.; Sun, M.; Duan, X.; Sun, H.; Li, P.; Wang, S. Zn phthalocyanine/carbon nitride heterojunction for visible light photoelectrocatalytic conversion of CO₂ to methanol. *J. Catal.* **2019**, *371*, 214–223. [[CrossRef](#)]
30. Bottari, G.; Trukhina, O.; Ince, M.; Torres, T. Towards artificial photosynthesis: Supramolecular, donor-acceptor, porphyrin- and phthalocyanine/carbon nanostructure ensembles. *Coordin. Chem. Rev.* **2012**, *256*, 2453–2477. [[CrossRef](#)]
31. Zhu, Z.; Lu, W.; Li, N.; Xu, T.; Chen, W. Pyridyl-containing polymer blends stabilized iron phthalocyanine to degrade sulfonamides by enzyme-like process. *Chem. Eng. J.* **2017**, *321*, 58–66. [[CrossRef](#)]
32. Zhang, W.; Zhou, X.; Huang, J.; Zhang, S.; Xu, X. Noble metal-free core-shell CdS/iron phthalocyanine Z-scheme photocatalyst for enhancing photocatalytic hydrogen evolution. *J. Mater. Sci. Technol.* **2022**, *115*, 199–207. [[CrossRef](#)]
33. Zhang, F.; Yi, J.; Peng, W.; Radjenovic, P.; Zhang, H.; Tian, Z.; Li, J. Elucidating molecule-plasmon interactions in nanocavities with 2 nm spatial resolution and at the single-molecule level. *Angew. Chem. Int. Ed. Engl.* **2019**, *58*, 12133–12137. [[CrossRef](#)] [[PubMed](#)]
34. Liang, Q.; Zhang, M.; Liu, C.; Xu, S.; Li, Z. Sulfur-doped graphitic carbon nitride decorated with zinc phthalocyanines towards highly stable and efficient photocatalysis. *Appl. Catal. A Gen.* **2016**, *519*, 107–115. [[CrossRef](#)]
35. Liu, Z.; Wan, J.; Yang, Z.; Wang, S.; Wang, H. Copper phthalocyanine-functionalized graphitic carbon nitride: A hybrid heterostructure toward photoelectrochemical and photocatalytic degradation applications. *Chem. Asian J.* **2016**, *11*, 1887–1891. [[CrossRef](#)]
36. Yuan, A.; Lei, H.; Wang, Z.; Dong, X. Improved photocatalytic performance for selective oxidation of amines to imines on graphitic carbon nitride/bismuth tungstate heterojunctions. *J. Colloid Interf. Sci.* **2020**, *560*, 40–49. [[CrossRef](#)]
37. Yao, C.; Yuan, A.; Wang, Z.; Lei, H.; Zhang, L.; Guo, L.; Dong, X. Amphiphilic two-dimensional graphitic carbon nitride nanosheets for visible-light-driven phase-boundary photocatalysis. *J. Mater. Chem. A* **2019**, *7*, 13071–13079. [[CrossRef](#)]
38. Christendat, D.; David, M.; Morin, S.; Lever, A.; Kadish, K.; Shao, J. Synthesis and characterization of highly soluble hexadecachloro- and hexadecafluorophthalocyanine ruthenium (II) complexes. *J. Porphyr. Phthalocya.* **2005**, *9*, 626–636. [[CrossRef](#)]
39. Qian, J.; Shen, C.; Yan, J.; Xi, F.; Dong, X.; Liu, J. Tailoring the electronic properties of graphene quantum dots by P doping and their enhanced performance in metal-free composite photocatalyst. *J. Phys. Chem. C* **2017**, *122*, 349–358. [[CrossRef](#)]

40. Han, X.; Yuan, A.; Yao, C.; Xi, F.; Liu, J.; Dong, X. Synergistic effects of phosphorous/sulfur co-doping and morphological regulation for enhanced photocatalytic performance of graphitic carbon nitride nanosheets. *J. Mater. Sci.* **2018**, *54*, 1593–1605. [[CrossRef](#)]
41. Yang, Q.; Yang, W.; He, F.; Liu, K.; Cao, H.; Yan, H. One-step synthesis of nitrogen-defective graphitic carbon nitride for improving photocatalytic hydrogen evolution. *J. Hazard Mater.* **2021**, *410*, 124594. [[CrossRef](#)] [[PubMed](#)]
42. Wang, Q.; Li, H.; Yang, J.; Sun, Q.; Li, Q.; Yang, J. Iron phthalocyanine-graphene donor-acceptor hybrids for visible-light-assisted degradation of phenol in the presence of H₂O₂. *Appl. Catal. B Environ.* **2016**, *192*, 182–192. [[CrossRef](#)]
43. Zeng, P.; Zhang, W.D. Photocatalytic hydrogen evolution over a nickel complex anchoring to thiophene embedded g-C₃N₄. *J. Colloid. Interface Sci.* **2021**, *596*, 75–88. [[CrossRef](#)] [[PubMed](#)]
44. Yuan, A.; Lei, H.; Xi, F.; Liu, J.; Qin, L.; Chen, Z.; Dong, X. Graphene quantum dots decorated graphitic carbon nitride nanorods for photocatalytic removal of antibiotics. *J. Colloid Interface Sci.* **2019**, *548*, 56–65. [[CrossRef](#)]
45. Bao, J.; Jiang, X.; Huang, L.; Quan, W.; Zhang, C.; Wang, Y.; Wang, H.; Zeng, Y.; Zhang, W.; Ma, Y.; et al. Molybdenum disulfide loading on a Z-scheme graphitic carbon nitride and lanthanum nickelate heterojunction for enhanced photocatalysis: Interfacial charge transfer and mechanistic insights. *J. Colloid Interface Sci.* **2022**, *611*, 684–694. [[CrossRef](#)]
46. Zhou, C.; Xu, P.; Lai, C.; Zhang, C.; Zeng, G.; Huang, D.; Cheng, M.; Hu, L.; Xiong, W.; Wen, X.; et al. Rational design of graphitic carbon nitride copolymers by molecular doping for visible-light-driven degradation of aqueous sulfamethazine and hydrogen evolution. *Chem. Eng. J.* **2019**, *359*, 186–196. [[CrossRef](#)]
47. Guo, F.; Chen, Z.; Shi, Y.; Cao, L.; Cheng, X.; Shi, W.; Chen, L.; Lin, X. A ragged porous hollow tubular carbon nitride towards boosting visible-light photocatalytic hydrogen production in water and seawater. *Renew. Energ.* **2022**, *188*, 1–10. [[CrossRef](#)]
48. Bao, X.; Lv, X.; Wang, Z.; Wang, M.; Liu, M.; Dai, D.; Zheng, L.; Zheng, Z.; Cheng, H.; Wang, P.; et al. Nitrogen vacancy enhanced photocatalytic selective oxidation of benzyl alcohol in g-C₃N₄. *Int. J. Hydrog. Energ.* **2021**, *46*, 37782–37791. [[CrossRef](#)]
49. Zhang, Y.; Zeng, P.; Yu, Y.; Zhang, W. Integration of nickel complex as a cocatalyst onto in-plane benzene ring-incorporated graphitic carbon nitride nanosheets for efficient photocatalytic hydrogen evolution. *Chem. Eng. J.* **2020**, *381*, 122635. [[CrossRef](#)]
50. Briggs, D.; Beamson, G. Primary and secondary oxygen-induced C_{1s} binding energy shifts in x-ray photoelectron spectroscopy of polymers. *Anal. Chem.* **1992**, *64*, 1729–1736. [[CrossRef](#)]
51. Ho, W.; Zhang, Z.; Lin, W.; Huang, S.; Zhang, X.; Wang, X.; Huang, Y. Copolymerization with 2,4,6-triaminopyrimidine for the rolling-up the layer structure, tunable electronic properties, and photocatalysis of g-C₃N₄. *ACS Appl. Mater. Interfaces* **2015**, *7*, 5497–5505. [[CrossRef](#)] [[PubMed](#)]
52. Li, K.; Sun, M.; Zhang, W. Polycyclic aromatic compounds-modified graphitic carbon nitride for efficient visible-light-driven hydrogen evolution. *Carbon* **2018**, *134*, 134–144. [[CrossRef](#)]
53. Russat, J. Characterization of polyamic acid/polyimide films in the nanometric thickness range from spin-deposited polyamic acid. *Surf. Interface Anal.* **1988**, *11*, 414–420. [[CrossRef](#)]
54. Duevel, R.; Corn, R. Amide and ester surface attachment reactions for alkanethiol monolayers at gold surfaces as studied by polarization modulation fourier transform infrared spectroscopy. *Anal. Chem.* **1992**, *64*, 337–342. [[CrossRef](#)]
55. Uchida, E.; Uyama, Y.; Iwata, H.; Ikada, Y. XPS analysis of the poly (ethylene terephthalate) film grafted with acrylamide. *J. Polym. Sci. Pol. Chem.* **1990**, *28*, 2837–2844. [[CrossRef](#)]
56. Yamashita, T.; Hayes, P. Analysis of XPS spectra of Fe²⁺ and Fe³⁺ ions in oxide materials. *Appl. Surf. Sci.* **2008**, *254*, 2441–2449. [[CrossRef](#)]
57. Hu, J.; Zhang, P.; An, W.; Liu, L.; Liang, Y.; Cui, W. In-situ Fe-doped g-C₃N₄ heterogeneous catalyst via photocatalysis-Fenton reaction with enriched photocatalytic performance for removal of complex wastewater. *Appl. Catal. B Environ.* **2019**, *245*, 130–142. [[CrossRef](#)]
58. Najdovski, I.; Selvakannan, P.; Bhargava, S.; O'Mullane, A. Formation of nanostructured porous Cu-Au surfaces: The influence of cationic sites on (electro)-catalysis. *Nanoscale* **2012**, *4*, 6298–6306. [[CrossRef](#)]
59. Liu, Y.; Yuan, A.; Xiao, Y.; Yu, H.; Dong, X. Two-dimensional/two-dimensional Z-scheme photocatalyst of graphitic carbon nitride/bismuth vanadate for visible-light-driven photocatalytic synthesis of imines. *Ceram. Int.* **2020**, *46*, 16157–16165. [[CrossRef](#)]
60. Han, X.; Yao, C.; Yuan, A.; Xi, F.; Dong, X.; Liu, J. Enhanced charge separation ability and visible light photocatalytic performance of graphitic carbon nitride by binary S, B co-doping. *Mater. Res. Bull.* **2018**, *107*, 477–483. [[CrossRef](#)]
61. Sivula, K. Mott-Schottky analysis of photoelectrodes: Sanity checks are needed. *ACS Energy Lett.* **2021**, *6*, 2549–2551. [[CrossRef](#)]
62. Liu, Y.; Liu, Y.; Xu, Y.; He, Q.; Yin, R.; Sun, P.; Dong, X. Phenanthroline bridging graphitic carbon nitride framework and Fe (II) ions to promote transfer of photogenerated electrons for selective photocatalytic reduction of nitrophenols. *J. Colloid Interface Sci.* **2022**, *608*, 2088–2099. [[CrossRef](#)] [[PubMed](#)]